



Title	Carbon Dioxide Decomposition by Plasma Methods and Application of High Energy and High Density Plasmas in Material Processing and Nanostructures
Author(s)	Srivastava, Mahesh P.; Kobayashi, Akira
Citation	Transactions of JWRI. 2010, 39(1), p. 11-25
Version Type	VoR
URL	<a href="https://doi.org/10.18910/6494">https://doi.org/10.18910/6494</a>
rights	
Note	

*The University of Osaka Institutional Knowledge Archive : OUKA*

<https://ir.library.osaka-u.ac.jp/>

The University of Osaka

# Carbon Dioxide Decomposition by Plasma Methods and Application of High Energy and High Density Plasmas in Material Processing and Nanostructures<sup>†</sup>

SRIVASTAVA Mahesh P.\*\* and KOBAYASHI Akira \*

## Abstract

*The increase of carbon dioxide (CO<sub>2</sub>) in the atmosphere can cause climatic and geographical changes which will destroy nature. In order to combat this destruction many researchers have attempted either decomposition of carbon dioxide or carbon dioxide sequestration so as to bring the carbon dioxide content down to 260 ppm in the atmosphere. In the present paper, we have summarized some of the earlier attempts at the decomposition of carbon dioxide. We give a detailed introduction about the gas tunnel type of plasma jet for the decomposition of carbon dioxide. However, in most of the earlier attempts, carbon dioxide decomposed into carbon monoxide which is highly poisonous and it is a drawback in these attempts. In order to circumvent this drawback we have proposed a scheme for decomposition of carbon dioxide using an array of high voltage electrode systems with which it may be possible to decompose carbon dioxide to its constituents. We will also present some of the results of material processing using the gas tunnel type plasma jet and high energy high density non equilibrium plasma under fusion conditions such as those prevailing in dense plasma focus (DPF) device.*

**KEY WORDS:** (Carbon Dioxide), (Decomposition), (Plasma Methods), (High Energy and High Density Plasmas), (Material Processing), (Nanostructures)

## 1. Introduction

From ancient times the content of oxygen and carbon dioxide has been found to be between 210 thousand and 260 ppm respectively. This balance of oxygen and carbon dioxide content in the atmosphere has been disturbed significantly due to the rapid increase in population and the consequent deforestation for catering the needs of this enormous population. It is well known that this development is considered to be increase by per capita expenditure of power. This increase may be due to an increase in burning fossil fuels, emission from vehicles, emissions of carbon dioxide from industries and thermal power station and due to other developmental activities. These are the main causes of the rise in atmospheric carbon dioxide. This rise in atmospheric carbon dioxide can cause increase in absorption of long wavelength radiation which is not fully re-emitted. This may have localized effects as well as global effects in the temperature of our earth. The atmospheric temperature increase may result in glaciers melting and sea level increasing which may lead to the interchanging of land and water borders and vice versa. This can cause

dramatic climatic and geographical changes-effecting land & water bodies and will destroy nature. Therefore, the reduction of carbon dioxide is an important research topic for many researchers. Two main techniques adopted for reduction of carbon dioxide level in the atmosphere are carbon dioxide sequestration in which carbon dioxide has to be buried deep into the earth and ocean and carbon dioxide decomposition in which it is to be decomposed into its constituents and recycled. Carbon dioxide decomposition will result in a reduction of the increase of atmospheric carbon dioxide. In addition the reaction products in carbon dioxide decomposition will also help in potential utilization in metallurgy, organic catalysis and hydrogen production and also in restoring the natural carbon resources.

In this article we have summarized the mechanical and chemical methods for carbon dioxide decomposition in section 2. These methods are applicable for the decomposition of a few tens of cubic centimeters of carbon dioxide. The plasma methods such as plasma assisted thermal decomposition, dielectric barrier discharge, RF discharge plasma, tunnel type plasma jet for decomposition of carbon dioxide are discussed in

<sup>†</sup> Received on June 11, 2010

\* Associate Professor

\*\* Professor, Univ. of Delhi

Transactions of JWRI is published by Joining and Welding Research Institute, Osaka University, Ibaraki, Osaka 567-0047, Japan.

section 3 and section 4. However, in most of earlier plasma methods the decomposition of carbon dioxide into carbon monoxide is a major concern. Consequently we propose a scheme for decomposition of carbon dioxide in which the carbon dioxide is decomposed to carbon and oxygen and is discussed in section 5. The use of a gas tunnel type plasma jet and dense plasma focus device for material processing is discussed in section 6. In the dense plasma focus (DPF) device a highly non equilibrium, high energy plasma is generated which gives rise to highly energetic ions and its use for phase change of materials, fabrication of thin films and fabrication of nanoparticles and nanostructures is discussed.

### 2. Different Methods of Decomposition of Carbon Dioxide

In this section we discuss some methods for the decomposition of carbon dioxide. In most of the methods carbon dioxide is decomposed into carbon monoxide and oxygen. The decomposition of carbon dioxide by Davis<sup>1)</sup> was done using carbon dioxide-argon gas mixture in a shock tube where temperature varies from 2600 to 11000K. The rate of decomposition of carbon dioxide by shock waves is monitored by observing the infrared radiation. When the shock wave passes through the system there is an initial rapid rise in the infrared emission which later decays exponentially. This exponential decay of the infrared emission shows the decomposition of carbon dioxide into carbon monoxide and oxygen.

In another study the rate and degree of carbon dioxide decomposition was investigated by Wada et.al<sup>2)</sup> by reducing magnetite using hydrogen gas in a quartz tube at 300°C. After reduction of magnetite the reaction cell was evacuated to remove the excess hydrogen, then carbon dioxide gas was injected which leads to carbon dioxide decomposition by reduced magnetite. The carbon dioxide decomposition proceeded more effectively on the prolonged Hydrogen-reduced magnetite. At a low reduction degree of magnetite, carbon dioxide was decomposed to carbon with oxygen-deficient magnetite (ODM). On the other hand, at a high reduction degree, the mixed solid phase of ODM and  $\alpha$ -Fe decomposed carbon dioxide to carbon, accompanying transformation of the mixed phase to the magnetite phase.

Alternatively it is possible to decompose the carbon dioxide using the phase transformation of the magnetite under ball milling<sup>3)</sup> instead of its reduction. In this, fine magnetite ( $\text{Fe}_3\text{O}_4$ ) powder was used as the starting material, in which no impurities or other phases are included. A part of the sample was placed in a ball-mill vial with stainless steel balls. The inner pressure was kept constant. Mechanical milling was performed for a long time using a high-energy vibration ball-milling machine. After milling, Fe and  $\alpha\text{Fe}_2\text{O}_3$  phases appear in addition to the magnetite phase, if continuous milling was done then the  $\alpha\text{Fe}_2\text{O}_3$  disappeared after some time and a FeO phase

appeared simultaneously. The magnetite content gradually decreased with milling. The carbon dioxide decomposition with the milled powder was carried out in a quartz tube which was heat treated in a horizontal furnace. The carbon content of the sample slightly increased with milling time indicating that the production of FeO phase contributed to carbon dioxide decomposition. After the decomposition sample contained graphite (or other types of carbon), undissolved Fe (both bcc and fcc structure) and  $\text{Fe}_3\text{O}_4$  phase.

Catalyzing effects of impregnated Rh, Pt and Ce on Ni (II)-bearing ferrite (NF) activated with hydrogen have been studied for carbon dioxide decomposition to carbon at 300 °C<sup>4)</sup>. In this study the metal impregnated NF (m-NF) samples was first prepared chemically. Then a portion of sample was placed in a quartz tube within an electric furnace, and hydrogen gas was passed over the NF or m-NF samples to activate the samples. The activation rate of the metal impregnated NF samples was about 1.6 times as large as that of the NF samples. NF and m-NF samples were activated until their weights decreased by 10% and allowed to oxidize while flowing the carbon dioxide gas. Then carbon dioxide gas was injected to react with activated sample. The rates of carbon dioxide decomposition using activated Rh, Pt and Ce materials were larger than that of the activated NF. The effect of metal impregnation on the activation and carbon dioxide decomposition increased in the order of  $\text{Ce} < \text{Pt} < \text{Rh}$ .

In another study the thermal decomposition of carbon dioxide in a dense mixed-conducting membrane reactor was reported by Jin et.al<sup>5)</sup>. In this study there is a coupling between the carbon dioxide decomposition and the partial oxidation of methane (POM). The perovskite-type oxide of SCFZ ( $\text{SrCo}_{0.4}\text{Fe}_{0.5}\text{Zr}_{0.1}\text{O}_3$ ) was used to construct the membrane reactor. A disk shaped SCFZ membrane between two gold rings was held in place by two quartz tubes. The gold rings were of same dimensions as those of the quartz tubes, which left an effective area for oxygen permeation. An inner quartz tube was used to introduce a gas mixture of carbon dioxide and helium to the lower chamber, while the other quartz tube was used to introduce a gas mixture of methane and argon to the upper chamber. In this reactor first the reaction of carbon dioxide decomposition took place and then the POM reaction occurred simultaneously (or methane reacted with oxygen that permeated through the membrane from the carbon dioxide decomposition, to produce hydrogen and carbon monoxide gas over supported transition metal catalysts). The main advantage is utilizing reasonable carbon dioxide as the oxygen source, which reduces the discharge of carbon dioxide into atmosphere. It was found that the carbon dioxide conversion increased with increasing the temperature and decreased with increasing the feed flow rates of carbon dioxide or with decreasing the feed flow rates of methane.

### 3. Decomposition of Carbon Dioxide Using Plasma Methods

In this section we discuss some of the plasma methods for carbon dioxide decomposition. One of the methods is reported by Huczko et.al<sup>6)</sup>, in which a plasma reactor consisting of a typical plasma torch attached to a quartz tube was used for carbon dioxide decomposition and is shown in **Fig. 1**. The plasma jet was generated by a d.c. arc discharge under atmospheric pressure.

In this experiment the thermal decomposition of carbon dioxide occurred in argon plasma where carbon dioxide decomposed into carbon monoxide and oxygen. The oxidation of the carbon monoxide begins but the further decomposition of carbon monoxide to carbon cannot be done using this method.

Radio-frequency (RF) plasma is one of the alternative techniques for the decomposition of carbon dioxide. Hsieh et.al<sup>7)</sup> proposed an RF plasma technique for decomposition of carbon dioxide. **Figure 2** shows the main components of the Hsieh's experimental equipment which include a vacuum pump, a gas introduction device (mass flow controllers), a RF power source (an excitation source producing electromagnetic radiation within radio frequencies for initiating and sustaining plasma) and a Fourier transform infrared (FTIR) spectrometer analysis system.

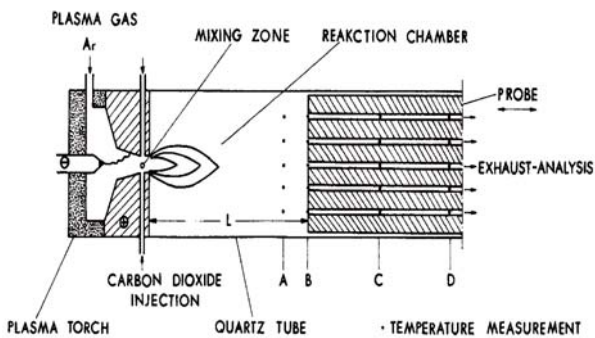


Fig. 1 Schematic of the plasma reactor.

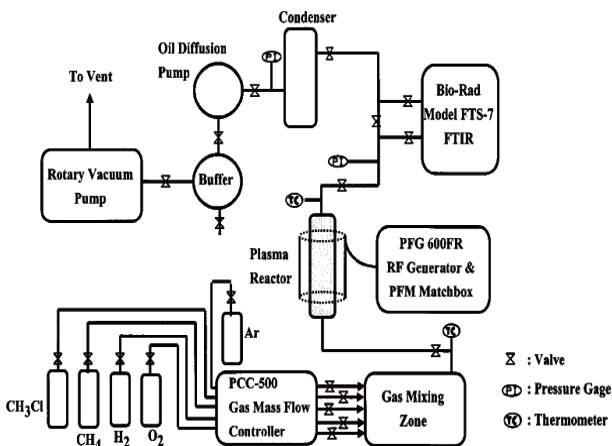


Fig. 2 Schematic diagram of experimental apparatus.

An RF plasma reactor was used in the experiment and a cylindrical vessel having an outer copper electrode wrapped on the plasma reactor and grounded. A 13.56 MHz RF power is connected to the outer copper electrode. The gas mixture was introduced from the bottom of the reactor which flows through glass tubes into the powered electrode zone. Under specific conditions one can observe that the decomposition fraction of carbon dioxide was 60.0%, which occurs around 316 °C.

In another study the decomposition of carbon dioxide using capacitive RF discharge was investigated by Sergey et.al<sup>8)</sup> over a moderate range of pressures (5-60 Torr) in a flowing plasma chemical reactor. Pure gas (or a mixture) went through the discharge tube, and after cooling down to room temperature, the product gases were analyzed by mass spectrometer. The schematic drawing of the experimental setup is shown in **Fig. 3**. In this experiment two kinds of plasma chemical reactors were used. One of them was a Pyrex discharge tube cooled using air flow from a ventilator. The second one was a quartz discharge tube positioned inside the oil-filled glass tube. A 13.56 MHz radio-frequency (RF) source is used for producing output power from 0 to 300 W.

In this experiment the decomposition of carbon dioxide is caused by direct electron collision via excitation of the unstable electronic state. Carbon monoxide was mainly produced from the decomposition of carbon dioxide. The decomposition of carbon dioxide in a plasma reactor was investigated experimentally by Mori et.al<sup>9)</sup>.

**Figures 4 and 5** show schematic diagrams of the experimental apparatus and the capillary plasma reactor, respectively. The capillary plasma reactor is a Pyrex glass tube connected to the gas inlet and outlet line by stainless-steel unions. The discharge tubes have two branch tubes for mounting the electrodes. The reactant gas flow does not contact the electrodes directly to eliminate the influence of the cathode and anode regions on carbon dioxide decomposition. Between the two electrodes, a dc voltage is applied and helium/carbon

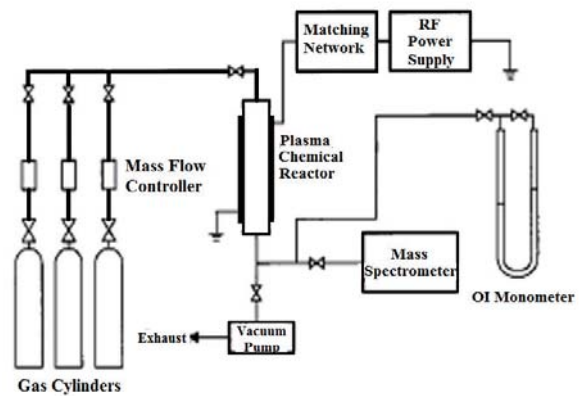


Fig. 3 Schematic drawing of experimental setup.

## Carbon Dioxide Decomposition by Plasma Methods and Application of High Energy and High Density Plasmas

dioxide plasma is generated in the capillary tube. Helium gas is used as a carrier gas to stabilize the capillary plasma for a wide range of discharge pressures and discharge currents. The chemical composition of the reaction products and the carbon dioxide conversion rates were studied. From this study one can deduce that the carbon dioxide conversion is predominately by the electron impact carbon dioxide dissociation and gas phase reverse reactions even in a capillary plasma reactor.

Decomposition of carbon dioxide to carbon monoxide and oxygen in argon stream under atmospheric pressure has been investigated by Matsumoto et.al.<sup>10)</sup> using a dielectric-barrier discharge plasma reactor (Fig. 6). In

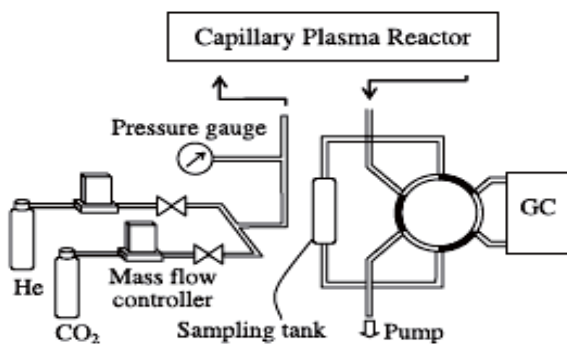


Fig. 4 Schematic diagram of experimental apparatus.

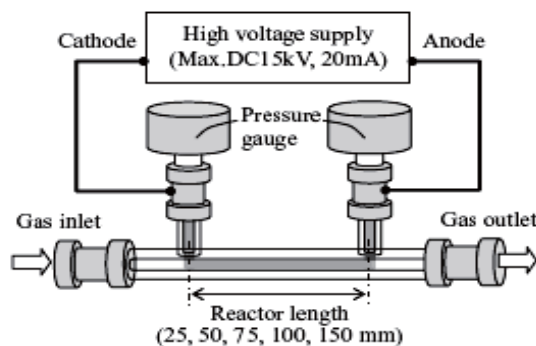


Fig. 5 Schematic diagram of capillary plasma reactor.

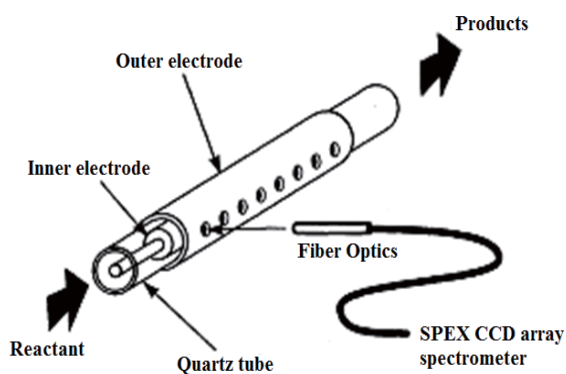


Fig. 6 Dielectric barrier discharge reactor.

this reactor the inner electrode was supported at the center by a quartz tube fitting. The quartz tube is used as the outer electrode tightly surrounded by a cylindrical jacket made by metallic aluminium. When an a.c. current at a high voltage was supplied into the argon stream, the homogeneous light of a cylindrical discharge was observed between the inner electrode and the quartz wall of the reactor tube. The carbon dioxide dissociation was found to proceed in accordance with the reaction  $2 \text{CO}_2 = 2 \text{CO} + \text{O}_2$  at considerable rates, which increased with increasing the input voltage, the carbon dioxide concentration in argon, and the heat of oxide formation of the corresponding metallic component used as the electrode.

Decomposition of carbon dioxide by a gliding arc plasma was examined by Indarto et.al.<sup>11)</sup>. The experimental setup consist of a plasma reactor made of a quartz-glass tube with a Teflon seal comprising two triangular electrodes made from stainless steel at upper part is shown in Fig. 7. The gas mixture was introduced between the electrodes through a capillary. A high frequency AC power supply was connected to the gliding arc electrode to generate plasma. The effect of total gas flow rates have been used to study the chemical process reaction in the gliding plasma system. The model of active-chemical kinetic carbon dioxide decomposition was developed to investigate the pathways of plasma reactions. In this study carbon dioxide decomposed to carbon monoxide and oxygen.

### 4. Decomposition of Carbon Dioxide Using Gas Tunnel Type Plasma Jet

In this section we discuss the plasma method which is being used for a number of times for carbon dioxide decomposition. In this method the plasma device used is a gas tunnel type plasma jet torch shown in Fig. 8. In this case carbon dioxide is inserted from the center hole of the cathode nozzle. Two d.c. power supplies were used for the generation of the gas tunnel type plasma jet.

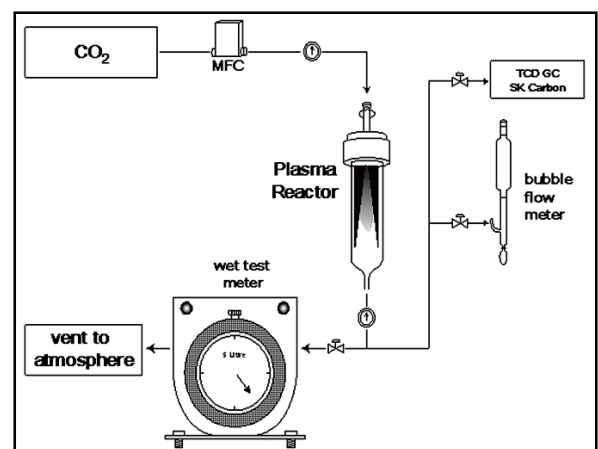


Fig. 7 Schematic diagram of experimental setup.

Argon was the main working gas and carbon dioxide and hydrogen gas were added to the reaction. Various modifications to this device for the better decomposition of carbon dioxide are reported elsewhere<sup>12-16</sup>. One of the modification to this device is a confront electrode type plasma jet (Fig. 9). In this case, the distance between the two electrodes is gradually bigger in the direction towards the torch exit thus it is easier to adjust the location of the electrode spot than the conventional plasma jet. This enables the working gas (as well as the plasma jet) to flow in an axial direction. This makes it superior to other plasma jets in terms of reactive performance. The major problem of this method is to enhance the performance for the effective reaction such as dissociation of carbon dioxide and synthesis of CH<sub>x</sub>.

The gas tunnel-type plasma jet was improved for a high-energy-type plasma jet shown in Fig. 10. The improvement was done in the ignition system (part A). The tungsten cathode for ignition was inserted from the hollow cathode of the gas tunnel-type plasma torch (part B) to the anode of the gas diverter nozzle before ignition, and pulled out after ignition by the high-frequency ignitor. Carbon dioxide gas was mixed with the working gas (argon) after the formation of the gas tunnel-type plasma jet. The experimental apparatus is shown in Fig. 11.

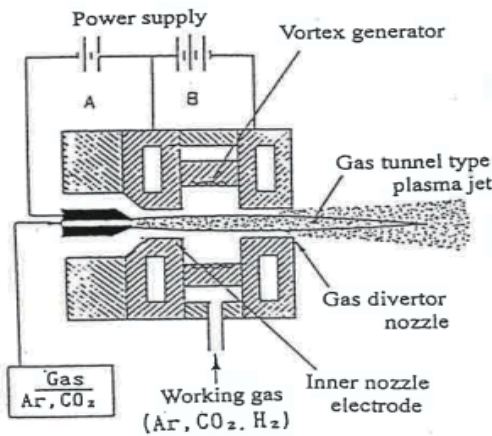


Fig. 8 Schematic of gas tunnel type plasma torch.

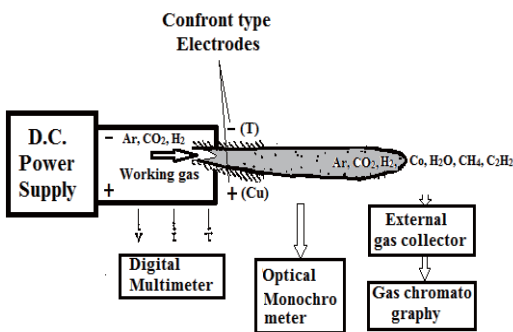


Fig. 9 Confront electrode type plasma jet.

The plasma torch is located at the center of the end wall of the cylindrical vacuum chamber. For the generation of the gas tunnel type plasma jet, a DC power supply was used, and argon was used as the plasma forming gas. For the purpose of this investigation, carbon dioxide and nitrogen gas were mixed with the working gas. The experiment was carried out under a vacuum pressure condition. The control of the plasma parameter was possible by changing experimental conditions. The exhaust gas from the plasma jet was collected at the wall of the exhaust tube to the vacuum pump by the gas collector. From the measurement of carbon monoxide and carbon dioxide contents, the efficiency of decomposition of carbon dioxide by the plasma jet was studied. The gas tunnel-type plasma jet was used to decompose carbon dioxide and the characteristics of this method were clarified by varying the plasma operating conditions.

The result revealed by the fundamental experiment is the arc voltage of the plasma torch was increased with increase in the carbon dioxide mixing ratio. The thermal efficiency of gas tunnel type plasma using the mixing gas was  $\eta = 65-80\%$ , as the mixing ratio was increased, higher efficiency was obtained. The thermal efficiency was increased as the power input to plasma torch was increased.

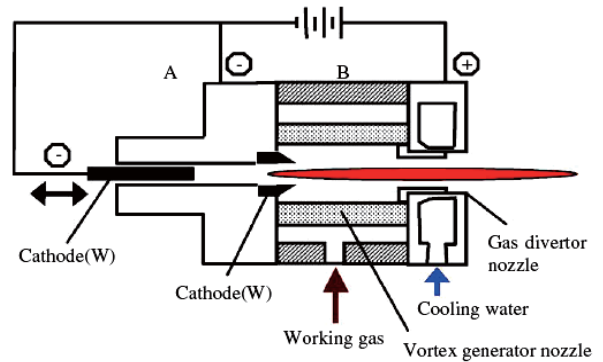


Fig. 10 Schematic of gas tunnel type plasma torch.

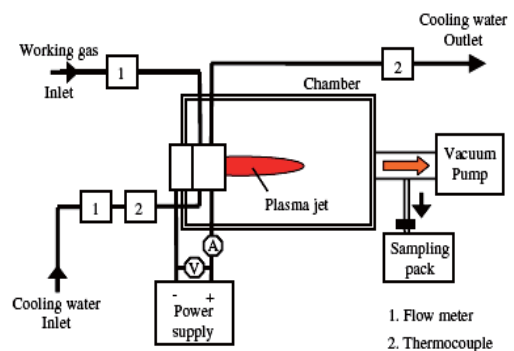


Fig. 11 Experimental arrangement for production of carbon dioxide by gas tunnel type plasma jet.

## Carbon Dioxide Decomposition by Plasma Methods and Application of High Energy and High Density Plasmas

The result of the performance test of the gas tunnel type plasma jet for decomposition of carbon dioxide showed that the thermal efficiency using mixed working gas was about  $\eta=65\%$  when the working gas flow rate of 100 l/min with the carbon dioxide content of 20% in the working gas and the discharge current of  $I=100A$ . The efficiency of carbon dioxide decomposition by the high energetic plasma jet was determined at various conditions. The optimum operating conditions of the gas tunnel type plasma jet will enhance its performance and improve the decomposition process of carbon dioxide. A high decomposition ratio of carbon dioxide will be realized at low carbon dioxide content when high power plasma is used. On the other hand, the decomposition amount per unit power was increased with increase in the mixing ratio of carbon dioxide.

### 5. Proposed Scheme of Carbon Dioxide Decomposition

The new scheme proposed is an approach to completely decompose carbon dioxide to its constituent carbon and oxygen by applying a very high potential to the 3D array of electrodes both horizontally all connected and vertically with alternating positive and negative terminals of high tension. The electrostatic shielding for each pair of vertical electrode is maintained. The experimental setup for this scheme is shown in **Fig. 12**. The direction of the electric field is in the vertically upward direction of the chimney. Such a large electric field will dissociate carbon dioxide into carbon and oxygen which subsequently ionize into carbon and oxygen ions.

A constant magnetic field is applied in the plane perpendicular to the plane of the paper as shown. The magnetic field provides different larmor radii to carbon and oxygen ions which can be separately collected as is done in isotope separation of  $U^{235}$  from  $U^{238}$ , or the principle used in a mass spectrograph.

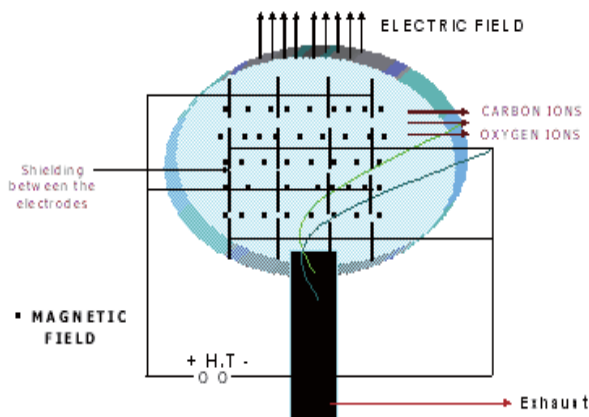


**Fig. 12** Proposed Set up for carbon dioxide decomposition.

### 6. Coating Using Gas Tunnel Type Plasma Jet and Material Processing Using Dense Plasma Focus Device

#### 6.1 Gas tunnel type plasma jet

The structure of gas tunnel type plasma jet is shown in Fig. 9. In this system the working gas makes a strong vortex flow in the chamber, and forms a low pressure gas tunnel along the torch center axis. This makes plasma production easier, and the strong vortex constricts and stabilizes the plasma jet. The gas tunnel type plasma jet is a high voltage type and also has a positive current-voltage characteristic. The plasma formed in this device is longer and more stable. The applications of this device in the coating are discussed briefly by means of thermal spraying.

#### 6.2 Gas tunnel type plasma spraying

In this application the spraying powder is fed inside the plasma flame in an axial direction from the central electrode of the plasma gun. Study of the characteristics of gas tunnel spraying<sup>17)</sup> indicated that the sprayed particles are in a fully molten state. As a result, the porosity is decreased, and mechanical properties, such as Vickers hardness, are improved. Therefore, a higher quality ceramic coating can be obtained by the gas tunnel plasma spraying method than with conventional plasma spraying. New functional materials have been produced by plasma spraying with potential in numerous technological applications<sup>18-19)</sup>.

##### 6.2.1 Ceramic coating

There are a number of problems with regard to the mechanical, electrical, chemical, and thermal properties of ceramic coatings produced by a conventional plasma spraying apparatus. These problems can be attributed to the fact that the spraying powder is usually supplied through an inlet located either at the torch exit or at the straight section of the anode nozzle. Moreover, with a conventional plasma spraying apparatus it is very difficult to supply the powder directly into the center of the plasma flame without damaging the electrodes or choking the nozzles. Thus the energy of the plasma jet cannot efficiently heat, melt, and accelerate the ceramic powder. The high-performance gas tunnel type plasma jet<sup>20)</sup> is characterized by a higher temperature, speed, and energy<sup>14-15)</sup>. The gas tunnel type plasma jet was used for high quality ceramics coating by Arata et. al.<sup>21)</sup>. The gas tunnel-type plasma jet solves the coating problems encountered with a conventional apparatus (**Fig.13** and **14**). Similar to the alumina coatings just discussed, the quality of stabilized zirconia coatings improved. Figure 13 shows two microstructures of zirconia coatings: (a) is the coating produced by a gas tunnel type plasma spraying apparatus and (b) is produced by conventional means. Zirconia powder has a very high melting point. Forming a coating with zirconia is therefore difficult, and zirconia coatings produced by conventional means are generally very porous, as can be seen in Fig. 13(b).

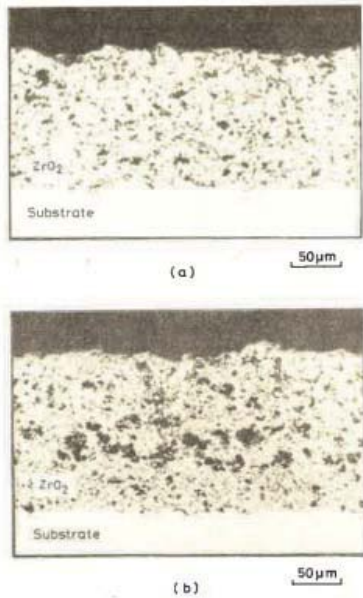


**Fig. 13** Microstructure of a zirconia coating. (a) gas tunnel type plasma spraying apparatus, (b) conventional plasma spraying apparatus.

Zirconia coatings produced with the gas tunnel-type plasma spraying apparatus exhibit much less porosity. It is therefore obvious that the quality of the sprayed coatings is superior to that of conventionally produced coatings since the fewer the pores, the greater the homogeneity of the coating. As a result of the reduced porosity zirconia coatings have very high quality characteristics than other coating materials.

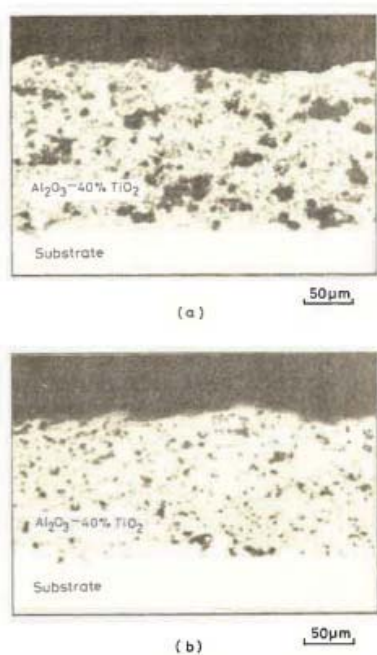


**Fig. 14** Microstructure of an alumina-titania coating. (a) gas tunnel type plasma spraying apparatus, (b) conventional plasma spraying apparatus.

### 6.2.2 Alumina coating

A high quality coating of alumina with a Vickers hardness of 1200 to 1600 HV have been obtained by gas tunnel plasma spraying<sup>22)</sup>. The gas tunnel plasma spraying was used for an alumina coating formed at a short spray distance, and the coating characteristics were discussed<sup>23)</sup>. The Vickers hardness of the cross section was measured for this alumina coating, and the effect of the spraying conditions (spraying distance, power input, etc.) on the properties of the alumina coating were also discussed.

The microstructure of such alumina coated material was examined by optical microscopy shown in **Fig. 15**. There are differences in the coating microstructure indicated as A, B, and C in Fig. 15. Regions A and B correspond to the high hardness region in which the distance from the surface is less than 300 µm and the Vickers hardness is more than 1000 HV. This coating region was formed during the second and third passes of the torch. In region B, the cell size is small compared to the other regions and forms a layer that is ~60 µm thick, which corresponds to the hardness >1300 HV. On the other hand, for region A near the coating surface, the cell size is greater. In this region, the hardness is a little lower than that in area B. Closest to the substrate, region C corresponds to the first torch pass. This region has the same coating structure as that formed by gas tunnel plasma spraying at the usual spraying distance. Region C is formed during the first traverse and consists of an upper dark layer that is γ-alumina rich and a lower layer near the substrate that is a bright, α-alumina rich area. The brightness increases considerably on the coating over region C. Region B has a fine structure and is the brightest indicating that this layer has a high concentration of α-alumina.

Region A, near the surface and formed on the third pass of the torch, has the highest brightness and indicates a high concentration of α-alumina. Regions under A are slightly darker and indicate a mixture of α-alumina and γ-alumina phases. The ratio of α-alumina and γ-alumina is nearly constant for the whole coating, which corresponds to the flat distribution of the Vickers hardness in the thickness direction.

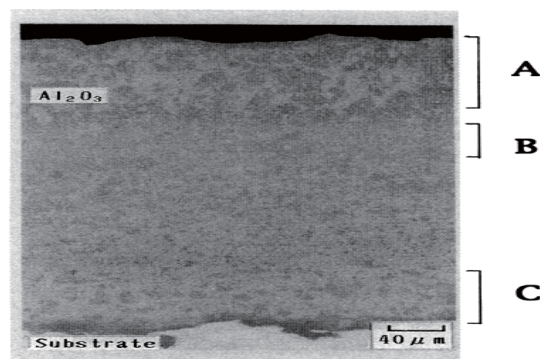


**Fig. 15** Microstructure of an alumina coating. The thickness of this coating is about 450 µm.

### 6.3 Dense plasma focus device

Bottom up as well as a hybrid approach for the nanofabrication can be achieved by plasma methods in the laboratory. Recently, it has been established that plasma aided nanofabrication<sup>24-26)</sup> is among the best methods of forming nanostructures. It has been established<sup>24-25)</sup> that ions generated by high density, high temperature and extremely non-equilibrium plasma of Dense Plasma Focus (DPF)<sup>27)</sup> can be used for nanofabrication of materials without dc biasing, heating of substrate or annealing. Though it was believed earlier<sup>26)</sup> that the ions produced in high temperature, high density and strongly non-equilibrium plasma such as prevailing under fusion conditions are not useful for material processing and nanofabrication.

DPF device is well known to produce a high density ( $10^{26} \text{ m}^{-3}$ ) and high temperature (1-2 KeV) pulsed plasma for a duration of  $\sim 100 \text{ ns}$ . The DPF device makes use of highly energetic, high fluence ions of the gas as well as of the material of which top of the anode is made. DPF device is also a cost effective, reduces the energy consumption with less treatment time over the other methods. Earlier DPF was used for phase change of materials<sup>28-32)</sup> and fabrication of thin films<sup>33-35)</sup>. Recently, the ions generated in DPF device are used for fabrication of nanoparticles<sup>24-25, 36-42)</sup>.

#### 6.3.1 Experimental procedure

An arrangement of the experimental system along with the electrode system and plasma chamber is shown in **Fig. 16**.

A 3.3 KJ Mather type DPF device, powered by 30  $\mu\text{F}$ , 15 KV fast discharging energy storage capacitor is used

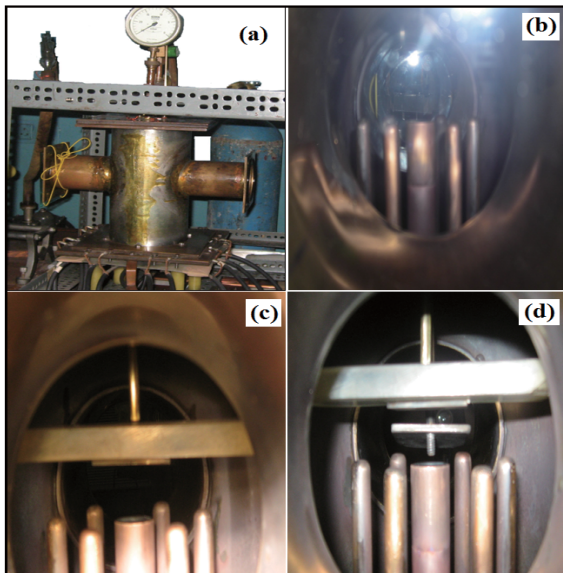


**Fig. 16** (a) The plasma chamber from outside, (b) the electrode assembly of the DPF device, (c) electrode assembly with substrate holder, (d) electrode assembly with substrate holder and shutter.

for obtaining nanomaterials. The vacuum chamber (Fig. 16(a)) consists of a single anode rod at the centre surrounded by six cathode rods in a squirrel-cage like structure (Fig. 16(b)). In this series of experiments, the anode of the electrode assembly has been modified with a detachable arrangement on the top to host the cylindrical disc of the material to be deposited. Discs of material to be fabricated having diameters equal to the inner diameter of the anode were made. The discs were then inserted at the top of the modified anode.

The substrates were cleaned and mounted on a substrate holder (Fig. 16(c)). A shutter is placed above the anode and slightly below the substrates (Fig. 16(d)) which protects the substrates from the impact of unfocused energetic ions at the beginning of the experiment. The focus chamber is evacuated by a rotary pump before admitting the argon gas. The DPF device is operated at an optimum pressure of 80 Pa to ensure good focusing. A 30  $\mu\text{F}$  capacitor is charged to about 15KV by a high voltage charger and is discharged through the electrode assembly with the help of fast switching system and triggering circuit. The gas breakdown occurs between anode and cathode near the insulating sleeve. Image charges on the insulator sleeve initiate the discharge between the anode and the cathode forming weak current filaments leading to current densities having an axially downward component. The current in the anode creates an azimuthal magnetic field. The current filament then moves outwards due to radially outward Lorentz force arising due to axially downward component of current density and azimuthal magnetic field resulting in an inverse pinch phase. The current filament reaches the cathode due to this Lorentz force. As soon as the current sheath reaches the cathode the current filament has a dominant radial component of current density. The radial component of current density and azimuthal magnetic field gives rise to axially upward component of Lorentz force which is responsible for axial phase of current sheath. This takes the current sheath towards the top of the electrode assembly. At the top of the anode, axially upward component of current density becomes dominant and this along with the azimuthal magnetic field gives rise to a Lorentz force whose direction is radially inward causing the pinching of the plasma. The current sheath is accelerated towards the axis of the anode and the plasma collapses to form a thin column of hot, dense plasma at the top of the anode. This is the focused phase having an electron density of the order of  $10^{26} \text{ m}^{-3}$  and temperature 1-2 KeV.

After getting good focus, which is evident as a spike in the voltage probe signal in the digital storage oscilloscope (Tektronix TDS 784), the disc placed at the top of the anode is brought into an ionized state by high density, high temperature plasma producing material ions. These ions along with the gas ions move vertically upward in a fountain shape in the post focus phase. These ions then condense on the substrates placed above the top of the anode.

Now, I describe the important features of plasma processing of nanomaterials under extremely non equilibrium plasma conditions prevailing in Dense Plasma Focus (DPF) device. Material in the form of pellet or disc is needed for fixing it at the top of the anode. A pellet of material is made using powder, grinding and palletizing it. The pellet is then sintered at 700 °C in a furnace. A disc of material is made using the rod or foil of the material. This pellet or disc is fitted at the top of modified anode.

### 6.3.2 Phase change of magnetite from hematite using ions generated in DPF

In the present work, the iron oxide ( $\alpha$ -Fe<sub>2</sub>O<sub>3</sub>) films have been irradiated by energetic argon ions. These films have been prepared by spin coating on glass substrate, using the gel obtained from iron (III) nitrate as precursor and 2-methoxy ethanol as solvent  $\alpha$ -Fe<sub>2</sub>O<sub>3</sub> films, having thicknesses of about 0.6  $\mu$ m on a glass substrate, are irradiated at different heights from the top of the anode. Typical results for films irradiated at distances of Z = 8, 9, 10 and 11 cm are discussed in the present work.

The XRD spectra of unexposed and ion irradiated films at heights of Z= 8, 9, 10 and 11 cm are shown in **Fig. 17**. The thickness of the unexposed film is of the order of 0.60  $\mu$ m. The XRD spectrum of the film without irradiation (Fig. 17(a)) shows a sharp peak at  $2\theta = 33.1^\circ$  indicating the most prominent peak of non-magnetic, hexagonal  $\alpha$ -Fe<sub>2</sub>O<sub>3</sub> phase. The thickness of the film irradiated at Z = 8 cm from the top of the anode is less than 0.1  $\mu$ m. At this height, most of the  $\alpha$ -Fe<sub>2</sub>O<sub>3</sub> has been removed by the impact of argon ions.

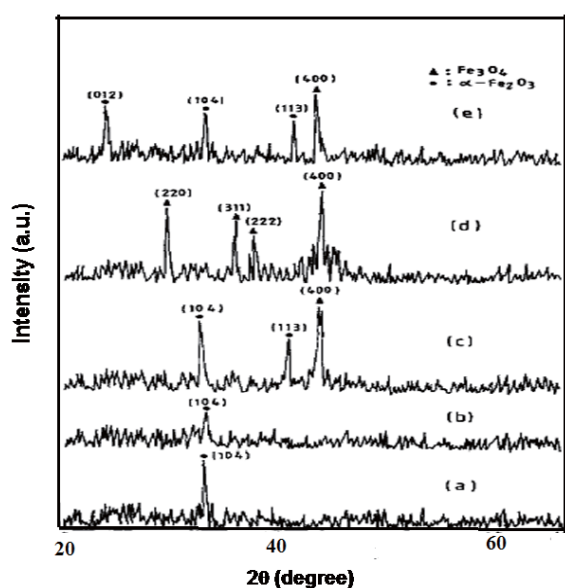


**Fig. 17** X-ray diffraction pattern for (a) unexposed film and ion irradiated films at (b) Z= 8.0 cm. c) Z= 9.0 cm, (d) Z= 10.0 cm and (e) Z= 11.0 cm.

The XRD pattern of this film (Fig. 17(b)) shows an appreciable reduction in intensity corresponding to the peak of  $\alpha$ -Fe<sub>2</sub>O<sub>3</sub>. The thickness of the film irradiated at Z= 9 cm is found to be about 0.13  $\mu$ m. The XRD of this film is shown in Fig. 17(c). The peaks having hkl values (104) and (113) at  $2\theta$  equal to  $33.14^\circ$  and  $40.5^\circ$  respectively correspond to  $\alpha$ -Fe<sub>2</sub>O<sub>3</sub> and the doublet at about  $2\theta = 43.5^\circ$  and  $43.2^\circ$  shows the presence of both  $\alpha$ -Fe<sub>2</sub>O<sub>3</sub> and Fe<sub>3</sub>O<sub>4</sub> phase. The thickness of the film irradiated at Z = 10 cm is found to be about 0.26  $\mu$ m. The XRD of this film is shown in Fig. 17(d). The peaks are observed at  $2\theta$  equal to  $30.1^\circ$ ,  $35.6^\circ$ ,  $37.4^\circ$  and  $43.2^\circ$ . These peaks correspond to hkl values (220), (311), (222) and (400) respectively and suggest the presence of magnetic, cubic Fe<sub>3</sub>O<sub>4</sub> phase. The absence of all peaks of  $\alpha$ -Fe<sub>2</sub>O<sub>3</sub> in the spectrum shown in Fig. 17(d) suggests a complete change of phase to Fe<sub>3</sub>O<sub>4</sub>. The finger print line from the (222) plane provides further confirmation of the Fe<sub>3</sub>O<sub>4</sub> phase. The thickness of the film irradiated at Z = 11 cm is found to be about 0.54  $\mu$ m. Fig. 17(e) shows the XRD of this sample having peaks at  $2\theta = 24.18^\circ$ ,  $32.9^\circ$ ,  $40.9^\circ$  of  $\alpha$ -Fe<sub>2</sub>O<sub>3</sub> and at  $2\theta = 43.0^\circ$  of Fe<sub>3</sub>O<sub>4</sub> which indicates the presence of both  $\alpha$ -Fe<sub>2</sub>O<sub>3</sub> and Fe<sub>3</sub>O<sub>4</sub> phase.

### 6.3.3 Thin films of materials deposited using DPF device a) CdS

The amorphization of as-grown crystalline thin film of CdS fabricated using DPF device. The energetic ions produced in DPF have been used to irradiate the thin films of CdS which have been obtained by depositing CdS on a glass substrate by the vacuum evaporation technique. The as-grown crystalline CdS films mounted on a sample holder were inserted in a plasma chamber and placed at heights of Z = 10, 8, 6, 4.2 and 2.5 cm from the top of the anode each time and were irradiated by means of energetic argon ions. The X-ray diffraction pattern of as-grown crystalline thin films of CdS is shown in **Fig. 18**. Changes in the surface morphology have been studied by utilizing a scanning electron microscope for the irradiated CdS film shown in **Fig. 19**.

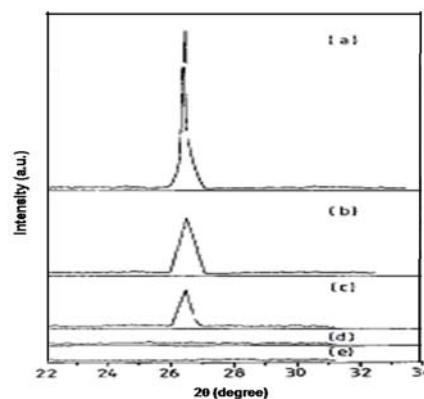


**Fig. 18** XRD spectrum of as-grown crystalline CdS film after irradiation at Z=4.2 cm.

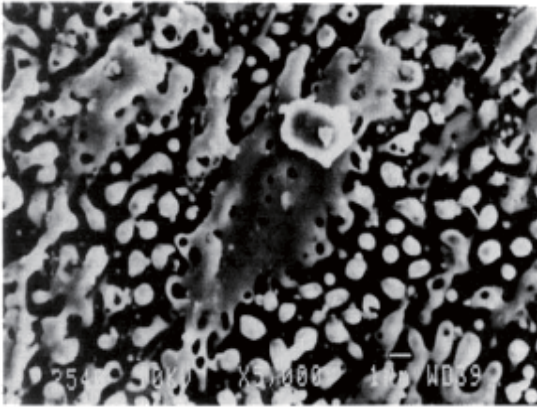


**Fig. 19** SEM of as-grown crystalline film of CdS after irradiation at (a) Z=10 cm, (b) Z=8 cm, (c) Z=6 cm, (d) Z=4.2 cm, (e) Z=2.5 cm.

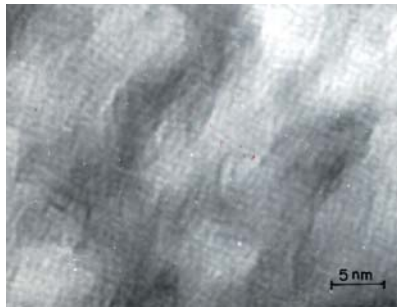


**Fig. 20** HRTEM of fullerene film.

**b) Fullerene**

The highly energetic and high fluence argon ions emitted in a dense plasma focus device are used to deposited fullerene films by ablating the graphite target such that the ablated material is deposited on a Si (111) substrate. These films have been studied using high resolution transmission electron microscope (HRTEM). To prepare the films silicon substrates are placed at a distance of 5.0 cm from the central anode and ten focused shots deposited on it. The HRTEM image is shown in **Fig. 20**. It shows the size of nanoparticles is of the order of 0.7 nm.

**c) Carbon**

Thin films of carbon are deposited on silicon, quartz and glass substrates keeping the target at different distances (like 1.3, 2.3 and 3.3 cm) above the anode and also varying the number of shots ( $n = 10, 20$  and  $30$ ). The deposition of the films was carried out for two different orientations of the substrate with respect to the target. In the first orientation, the substrate was placed parallel to the axis of the anode and at a distance of 1 cm opposite to the center of the graphite target. In the second orientation the substrate was placed parallel to the target making an

angle of  $45^\circ$  with the anode axis at a distance of 1 cm from the center of the graphite target. Visual inspection of the film shows a clearly distinct upper portion having a transparent, uniform brownish thin film on the substrate and a lower portion having a grayish hazy patch due to the deposition of macro particles. The thickness of the films was found to be in the range  $1000 - 1500 \text{ \AA}$ . It was found that the roughness average of the films deposited with the second orientation of the substrate was less as compared to the first orientation.

**6.3.4 Lead zirconate titanate (PZT)**

The PZT thin film has been deposited on the glass substrates using the ions generated in the DPF device. The PZT disc is formed in a solid state reaction and the materials initially taken are  $\text{ZrO}_2$ ,  $\text{TiO}_2$  and  $\text{PbO}$ . To form  $\text{Pb}(\text{Zr}_{0.53}\text{Ti}_{0.47})\text{O}_3$ ,  $\text{ZrO}_2$ ,  $\text{TiO}_2$  and  $\text{PbO}$  are taken as 53 mol%, 47 mol% and 110 mol%, respectively. The additional 10 mol% of  $\text{PbO}$  has been taken to compensate for the Pb loss, which takes place while depositing films. The three powders are mixed, ground to a fine powder and pressed into a disc of 15 mm diameter and 5 mm thickness. It is preheated at  $850^\circ\text{C}$  for 3 h. The disc is ground to a fine powder and again pressed into a disc this disc is sintered at  $950^\circ\text{C}$  for 2 h. Glass substrates are placed at a distance of 4.2 cm from the central anode then ten focused shots deposited on glass substrate. The surface morphology has been studied by utilizing a High resolution transmission electron microscope (HRTEM) image shown in **Fig. 21**. The average size of nanoparticles is found to be of the order of 0.5 nm.

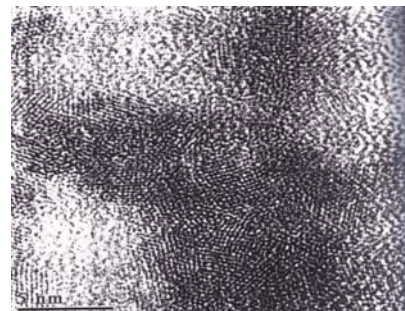


**Fig. 21** HRTEM of PZT.

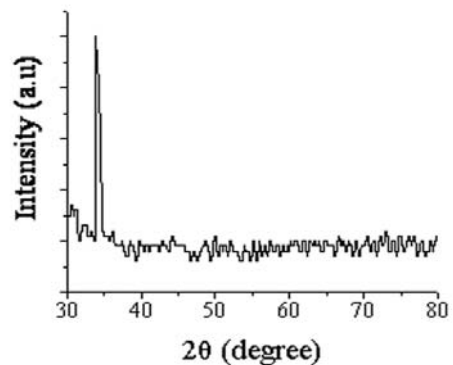


**Fig. 22** XRD image of ZnO nanoparticles.

### 6.3.5 Nanoparticles

#### a) Zinc oxide nanoparticles

Zinc Oxide (ZnO) is fabricated using pellets of ZnO. The substrates used are silicon which is placed at a distance of 5.0 cm from the top of the anode and two focused DPF shots are used.

The XRD spectra were obtained for showing the structural properties. **Figure 22** shows the XRD of material deposited. It shows a peak at  $34.6^\circ$  which correspond to [102] plane of ZnO.

In order to understand the surface morphology AFM image of ZnO nanoparticles is given in **Fig. 23**. The typical line analysis of AFM image of aluminium nanoparticles gives a roughness average (Ra), maximum height of the profile above the mean line (Rp), mean of maximum height above mean line (Rpm), maximum peak-to-valley height (Rt) and mean of peak-to-valley height (Rtm) to be 5.53 nm, 14.46 nm, 5.62 nm, 27.34 nm and 14.48 nm respectively. In order to understand the optical properties Photoluminescence (PL) was done for excitation wavelength of 334 nm and 355 nm. The PL results of excitation wavelengths of 334 nm are presented in **Fig. 24** as most of the emission peaks are observed at this wavelength for an excitation wavelength of 334 nm.

As can be seen in Fig. 24, shows UV emission with the characteristic energies of 3.41 eV (363 nm) and 3.26 eV (380 nm), blue visible emission with the energy peaks of 2.91 eV (427 nm), 2.71 eV (456 nm) and 2.55 eV (485 nm), as well as high-intensity green emission with the energy peak at approximately 2.38 eV (521 nm). The peak at 3.41 eV can be assigned to the excited

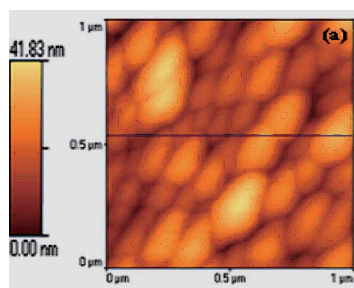


**Fig. 23** AFM image of ZnO nanoparticles.

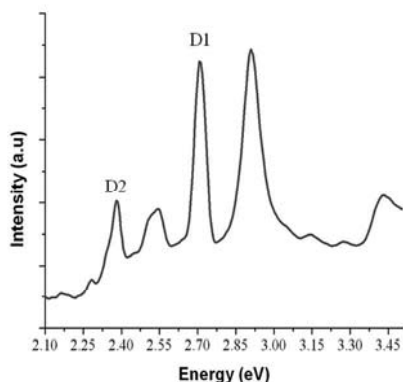


**Fig. 24** PL spectra of ZnO nanoparticles.

transition bound to neutral donor ( $D^0X$ ) sites and the peak at 3.26 eV is assigned to near-band-edge (NBE).

The emission peak at 2.55 eV (485 nm) can be assigned to the transition between an oxygen vacancy and peak at 2.91 eV and is due to an oxygen interstitial. It should be noted that emission peaks at 2.91 and 2.55 eV are not common to bulk zinc oxide. In zinc oxide, the energy level corresponding to anion vacancies lies approximately 2.7 eV (D1) below the conduction band whereas the energy level of the excited state of oxygen vacancies lies at  $\sim 2.4$  eV (D2). Therefore in the present study, the emission peaks observed at 2.38 eV (D2) and 2.71 eV (D1) can be associated with these two defect-related emission peaks.

#### b) Aluminium nanoparticles

In a similar manner Aluminium nanoparticles were prepared and characterized. Aluminium (Al) rod (99.999%) is used to form an Al disc. This disc is then fitted in the detachable anode. Aluminium is deposited on Si substrates placed at a distance of 4.0 cm for two focused DPF shots. The XRD pattern of Al deposited on n-Si substrate with few focused DPF shots shows a diffraction peak at  $2\theta = 44.8^\circ$  which corresponds to the (200) plane of aluminium. The atomic force microscope (AFM) image of aluminium nanoparticles is shown in **Fig. 25**. The typical line analysis of AFM image of aluminium nanoparticles gives Ra, Rp, Rpm, Rt and Rtm values of 7.52 nm, 22.70 nm, 10.56 nm, 42.45 nm and 23.17 nm respectively. Particles have diameter in the range of 40-80 nm.

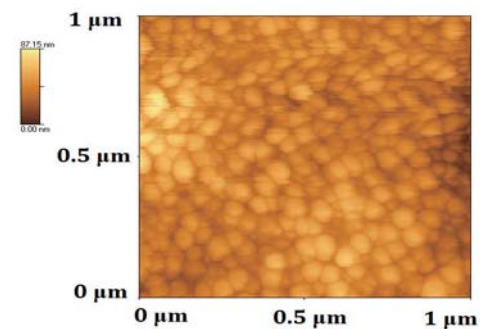


**Fig. 25** AFM image of Aluminium nanoparticles.

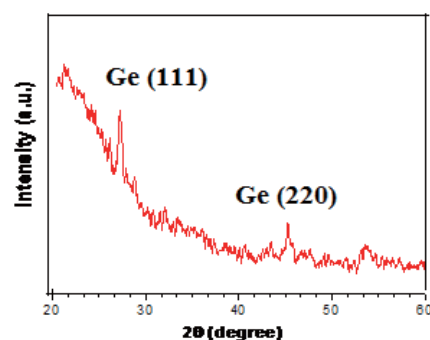


**Fig. 26** XRD of Germanium nanoparticles.

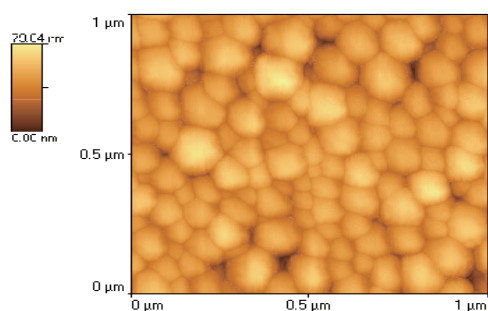


Fig. 27 AFM image of germanium nanoparticles.

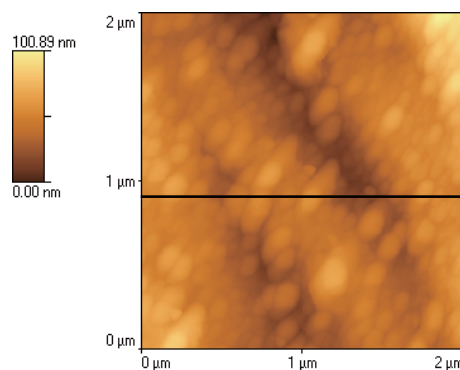


Fig. 29 AFM image of cobalt nanoparticles.

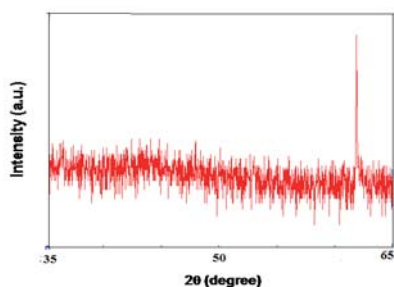


Fig. 28 XRD of Cobalt nanoparticles.

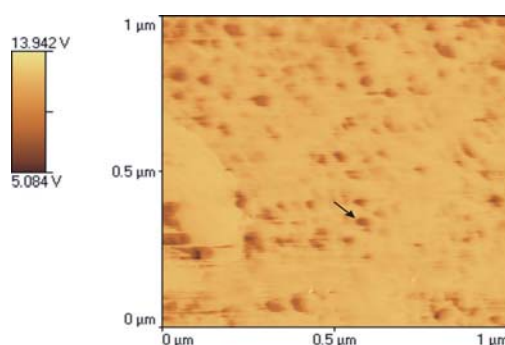


Fig. 30 MFM image of Cobalt nanoparticles.

**c) Germanium nanoparticles**

Germanium (Ge) material is prepared in the form of a disc using germanium rod (99.999%). This disc is then fitted in the detachable anode. Figure 26 shows the XRD for germanium nanoparticles that shows the (111) and (220) planes of germanium. The AFM image of Ge nanoparticles is shown in Fig. 27. Diameter of particles lies in the range of 40-100 nm. The typical line analysis of AFM image of Ge nanoparticles shows Ra, Rp, Rpm, Rt and to be 7.08 nm, 29.09 nm, 12.06 nm, 55.69 nm and 28.74 nm respectively.

**d) Cobalt nanoparticles**

Magnetic materials such as cobalt, iron nanoparticles were prepared and characterized. Cobalt disc is prepared using cobalt rod. This disc is then fitted in the detachable anode. The substrates were placed at a distance of 5.0 cm for three focused shots of DPF. X-ray diffraction of deposited cobalt is shown in Fig. 28.

It show a peak at 61.87° which correspond to [102] plane of hcp cobalt. The AFM image of cobalt nanoparticles is shown in Fig. 29. From a typical line analysis, we have found Ra, Rp, Rpm, Rt and Rtm to be 10.55 nm, 23.13 nm, 12.89 nm, 55.06 nm and 25.65 nm respectively. Figure 30 gives the magnetic phase image of cobalt nanoparticles deposited on Silicon substrate with three focused shots. The darker regions show the region of attractive force and lighter regions represent repulsive force of attraction between the tip and the sample surface. The typical size of magnetic domains (shown by arrow head) is about 10 nm.

**e) Iron nanoparticles**

Iron is deposited on quartz substrate placed at a distance of 5.0 cm from the top of the anode with two focused DPF shots. The AFM image is shown in Fig. 31.

From a typical line analysis, we have found Ra, Rp, Rpm, Rt and Rtm to be 3.19 nm, 6.65 nm, 4.23 nm, 16.36 nm and 8.87 nm respectively. The size of the particles was determined by critical dimension analysis and was found to be in the range of 20-80 nm with a typical particle size shown by arrowhead to be 40 nm.

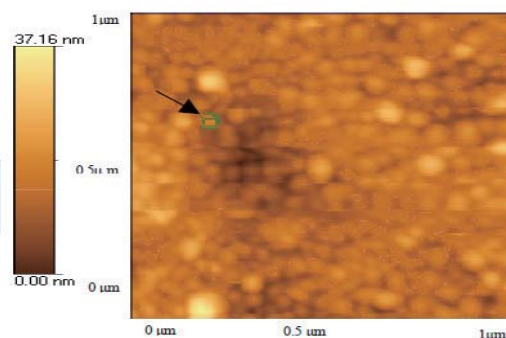


Fig. 31 AFM image of iron nanoparticles.

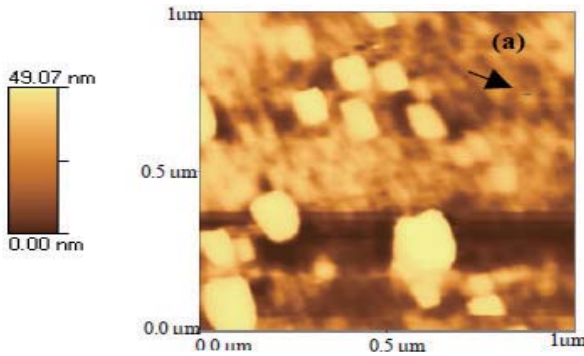


Fig. 32 MFM image of iron nanoparticles.

The topography image from MFM of Iron nanoparticles is shown in Fig. 32. The arrowhead in Fig. 12 shows a magnetic domain of typical dimension 40 nm. The image shows dark areas along with bright structures of approximately 100 nm which are randomly distributed all over the image.

6.3.6 Carbon nanoloops

In this study we have also heated the substrate and we found the formation of nanoloops. For this we have deposited a thin layer of nickel on quartz substrate for providing suitable nucleation of graphitic carbon nanostructures. The polished quartz substrates were mounted on the surface of a stainless steel resistive heater at a distance of 5cm from the top of the anode.

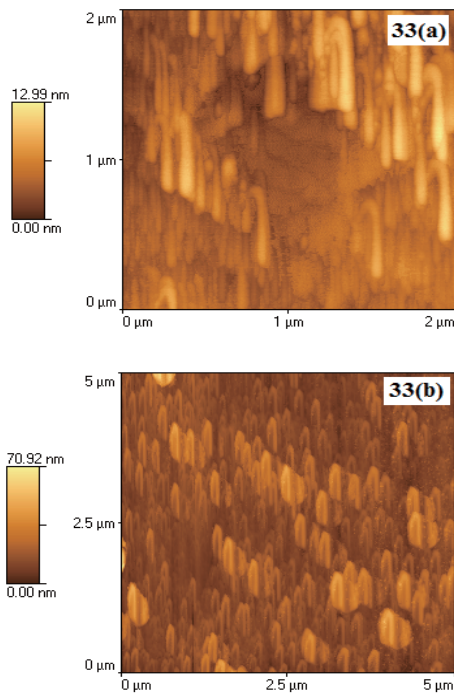


Fig. 33 AFM images at substrate temperatures of (a) 90 °C and (b) 94 °C.

Thermocouple is placed between lower surface of the substrate and the resistive heater. The substrate holder is fitted with a heater whose temperature was varied using a variac. The temperature of substrates is measured using a Cu-Constantan thermocouple. A layer of nickel was deposited on the quartz substrate by three focused shots. Subsequently, the nickel anode is replaced by a carbon anode and then five focused shots of graphitic carbon is deposited on the substrate. The experiment was carried out at substrate temperatures of 30 °C, 50 °C, 70 °C, 90 °C and 94 °C. We observe from AFM studies that there are no visible formations of nanoloops of carbon up to 70 °C. The samples deposited at 90 °C shown in Fig. 33(a) have the appearance of tubular structures having width in the range of 25 nm to 47 nm. At 94 °C we see the formation of carbon nanoloops as shown in Fig. 33(b).

6.3.7 Bilayer of cobalt-carbon

For observing the nucleation of nanostructures of graphitic carbon, a layer of magnetic material is deposited on the substrate.

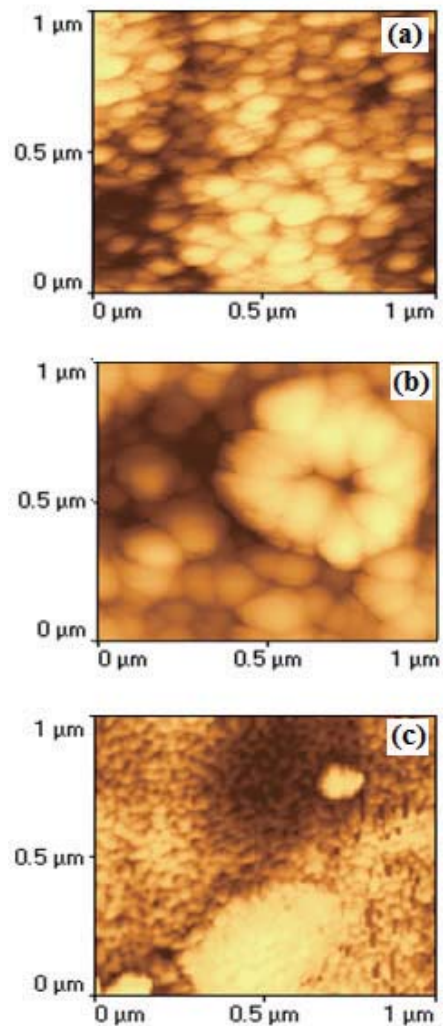


Fig. 34 AFM images of nanostructures of graphitic carbon with (a) one, (b) two and (c) three DPF shots from graphite disc.

A layer of cobalt was deposited on the silicon substrate by one focused shot. Subsequently, the cobalt anode is replaced by a carbon anode and then one, two and three focused shots of graphitic carbon are deposited on the substrate. AFM images of deposited graphitic carbon nanostructures with one focused shot of cobalt deposited on Si substrate with 1, 2 and 3 focused DPF shots from graphite disc are shown in Fig 34. The particles have radii in the range of 40-150 nm for 1 shot of graphite. The nanoparticles are scattered but as the number of shots increases to two, the particles combine to form a disc like structure which consists of many particles in the range of 40-150 nm as shown in Fig. 34.

As the number of DPF shots from graphite disc is increased to 3 the disc like structure is seen to crumble and a uniform deposition of graphite thin film as shown in Fig. 34(c). This may be due to the agglomeration of the particles forming different structures or this may be due to the condensation of ions on the substrates.

Figure 35 show the Raman spectra of graphitic carbon nanostructures deposited on Si substrate with 1 focused shot from cobalt disc and 1, 2, and 3 graphitic carbon DPF shots respectively. Fig. 35(a), Fig. 35(b) and Fig. 35(c) show G-bands at  $1532\text{ cm}^{-1}$ ,  $1582\text{ cm}^{-1}$  and  $1581\text{ cm}^{-1}$  for 1, 2 and 3 focused graphitic DPF shots respectively.

The D-band is observed only for 2 and 3 focused shots at  $1340\text{ cm}^{-1}$  and  $1350\text{ cm}^{-1}$  respectively. This band is assigned to disordered or defective structures of the crystalline phase of the material. Fig 35(c) also shows a peak at  $\sim 2705\text{ cm}^{-1}$  which correspond to a second-order 2D band.

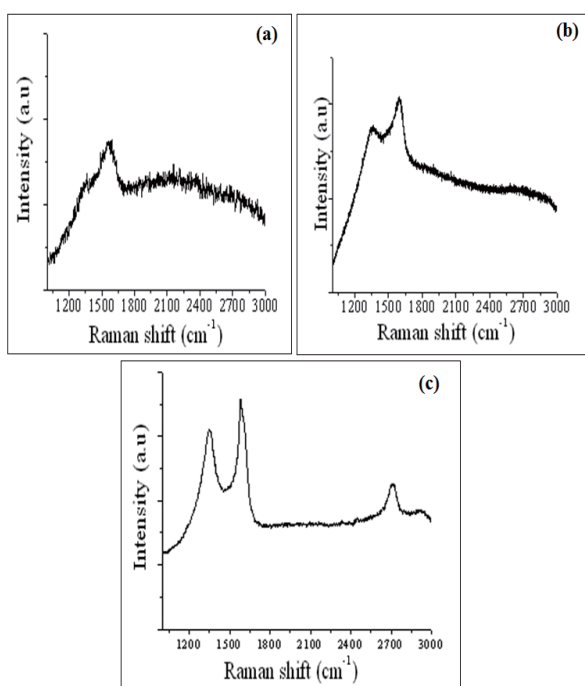


Fig. 35 Raman shift of graphitic carbon nanostructures with (a) 1, (b) 2 and (c) 3 DPF shots from graphite disc.

## Acknowledgement

Prof. M.P.Srivastava is grateful to JSPS, Japan for the award of Invitation Fellowship with the efforts of Prof. A. Kobayashi.

## References

- 1) W.O. Davis, *J. Chem. Phys.*, Vol. **43** No. **8**, (1965) pp.2809–2818.
- 2) Y.Wada, T. Yoshida, M. Tsuji and Y. Tamaura, *Energy Convers. Mgmt.*, Vol. **36**, (1995) pp.641–644.
- 3) E. Yamasue, H. Yamaguchi, H. Okumura, K.N. Ishihara, *J. of Alloys and Compounds*, Vol. **434–435**, (2007) pp.803–805.
- 4) M. Tsuji, T. Yamamoto, Y. Tamaura, T. Kodama and Y. Kitayama, *Applied Catalysis A: General*, Vol. **142**, (1996) pp.31–45.
- 5) W. Jin, C.Zhang, P. Zhang, Y. Fan, and N. Xu, *AIChE J.*, Vol. **52**, (2006) pp.2545–2550.
- 6) A. Huczko and A. szymanski, *Plasma Chem. and Plasma Proc.*, Vol. **4** No. 1, (1984) pp.59–71.
- 7) L.T. Hsieh, W-J Lee, C-T Li, C-Y Chen, Y-F Wang and M-B Chang, *J. Chem. Technol. Biotechnol.* Vol. **73**, (1998) pp.432–442.
- 8) S. Y. Savinov, H.Lee, H. K. Song, and B-K Na, *Ind. Eng. Chem. Res.* Vol. **38** (1999) pp.2540–2547.
- 9) S. Mori, A. Yamamoto and M. Suzuki, *Plasma Sources Sci. Technol.* Vol.**15**, (2006) pp.609–613.
- 10) H. Matsumoto, S. Tanabe, K.Okitsu, Y. Hayashi and S.L.Suib, *Bull. Chem. Soc. Jpn.* Vol. **72** (1999) pp.2567 – 2571.
- 11) A. Indarto *Asian Journal of Water, Environment and Pollution* Vol. **4** No. 1(2006) pp.191–194.
- 12) A. Kobayashi *Adv. in Appl. Plasma Sci.* Vol. **2** (1999) pp.269–275.
- 13) A. Kobayashi, K.Osaki and C. Yamabe *Vacuum* **65** (2002) pp.475–479.
- 14) Y.Arata and A. Kobayashi, *J. Appl. Phys.* Vol. **59** (1986) pp.3038–3044.
- 15) Y. Arata and A. Kobayashi, *Jpn. J. Appl. Phys.* Vol. **25** (1986) pp.1697–1701.
- 16) A. Kobayashi and H. Hamanaka, *Vacuum* Vol. **80** (2006) pp.1294–1298.
- 17) A. Kobayashi, S. Kurihara, Y. Habara and Y. Arata, *Q. J. Jpn. Weld. Soc.*, Vol **8**, (1990) pp.457–463.
- 18) J. Hasui, *J. Weld. Soc. Jpn.*, Vol.1.**37**, 1987, pp.52–58.
- 19) A. Kobayashi, *Weld. Int.*, Vol **4** (1990) pp.276–282.
- 20) Y. Arata and A. Kobayashi, *J. High Temp. Soc.*, Vol. **11** (1985) p.124.
- 21) Y. Arata, A. Kobayashi and Y. Habara, *J. Appl. Phys.*, Vol. **62** (1987) pp.4884–4889.
- 22) A. Kobayashi, Y. Habara and Y. Arata, *J. High Temp. Soc.*, Vol. **18** (1992) pp.89–96.
- 23) A. Kobayashi, *J. Thermal Spray Tech.*, Vol. **5** (1996) pp.298–302.
- 24) M. P. Srivastava, Ed. H.J. Kunze, T. El. Khalafawy, H. Hegazy, *Scheriften Des Forschungszentrum Julich GmbH* Vol. **34** (2003) pp.40–43.
- 25) M. P. Srivastava *Adv. in Appl Plasma Sci* Vol. **6** (2007) pp.227–230.
- 26) K. Ostrikov, *Reviews of Modern Physics* Vol. **77** (2005) pp.489–511.
- 27) J. W. Mather *Phys. Fluids* Vol. **7** (1964) pp 5.
- 28) R S Rawat, M P Srivastava, S Tandon and A Mansingh. *Phys. Rev B* Vol. **47** (1993) pp.4858–4862.

- 29) R Sagar and M P Srivastava, *Phys. Lett. A*. Vol. **183** (1996) pp.209-213.
- 30) M.P.Srivastava, et al. *Phys. Lett.A*. Vol.**215** (1996) pp.63-68.
- 31) P.Agarwal, M.P.Srivastava and R.S.Rawat, *Appl.Phys. Lett.* Vol.. **231** (1997) pp 434-438.
- 32) P Agarwal, M.P.Srivastava, P.N.Dheer, V.P.N.Padmanaban and A.K.Gupta, *Physica C*. Vol.**313** (1999) pp.87-92.
- 33) C. R. Kant, M.P Srivastava and R S Rawat, *Phys. Lett. A* Vol. **226** (1997) pp.212-216.
- 34) C.R.Kant, M.P.Srivastava and R.S.Rawat *Phys. Lett. A*. Vol. **239**, (1998) pp.109-114.
- 35) M P Srivastava and R Gupta, Eds. A Kobyashi and N M Ghoniem, *Adv. in Appl. Plasma Sci.* Vol. **2**, (1999) pp.161.
- 36) Ruby Gupta, M.P. Srivastava, V.R. Balakrishnan, R. Kodama and M.C. Paterson, *Journal of Phy D: Appl Phys* Vol.**37** (2004) pp.1091-1094.
- 37) Y. Malhotra, S.Roy, M.P.Srivastava, C.R.Kant, K.Ostrikov, *Journal of Phy D: Appl Phys* Vol. **42** (2009) pp.15202-09.
- 38) B.D.Naorem, S. Roy, M.P.Srivastava, *Adv. in Appl. Plasma Sci.* Vol. **7** (2009) pp.247-250.
- 39) B.D.Naorem, S.Roy, M.P.Srivastava, *Journal of Physics: CS* Vol. **208** (2010) 012103 (5pp).
- 40) W.P. Singh, S. Roy and M.P.Srivastava *J.Plasma Fusion Res. SERIES*, Vol. **8** (2009) pp.256-259.
- 41) W.P. Singh, S. Roy and M.P.Srivastava, *Journal of Physics:CS*, Vol. **208** (2010) 012105 (5pp).
- 42) Y. Malhotra and M.P.Srivastava *Adv. in Appl Plasma Sci.* Vol.**7** (2009) pp.255-257.